

# An Integrated System at the Bleien Observatory for Mapping the Galaxy

Chihway Chang,<sup>1\*</sup> Christian Monstein,<sup>1†</sup> Joel Akeret,<sup>1</sup> Sebastian Seehars,<sup>1</sup>  
Alexandre Refregier,<sup>1</sup> Adam Amara,<sup>1</sup> Adrian Glauser,<sup>1</sup> Bruno Stuber<sup>2</sup>

<sup>1</sup>*Institute for Astronomy, Department of Physics, ETH Zurich, Wolfgang-Pauli-Strasse 27, 8093 Zürich, Switzerland*

<sup>2</sup>*University of Applied Science, FHNW, Brugg, Switzerland*

\**chihway.chang@phys.ethz.ch*

†*monstein@astro.phys.ethz.ch*

27 July 2016

## ABSTRACT

We describe the design and performance of the hardware system at the Bleien Observatory. The system is designed to deliver a map of the Galaxy for studying the foreground contamination of low-redshift ( $z=0.13\text{--}0.43$ )  $\text{H I}$  intensity mapping experiments as well as other astronomical Galactic studies. This hardware system is composed of a 7m parabolic dish, a dual-polarization corrugated horn feed, a pseudo correlation receiver, a Fast Fourier Transform spectrometer, and an integrated control system that controls and monitors the progress of the data collection. The main innovative designs in the hardware are (1) the pseudo correlation receiver and the cold reference source within (2) the high dynamic range, high frequency resolution spectrometer and (3) the phase-switch implementation of the system. This is the first time these technologies are used together for a L-band radio telescope to achieve an electronically stable system, which is an essential first step for wide-field cosmological measurements. This work demonstrates the prospects and challenges for future  $\text{H I}$  intensity mapping experiments.

**Key words:** instrumentation, cosmology, HI intensity mapping, radio, calibration

## 1 INTRODUCTION

In the coming decades, a wealth of astronomical data in radio wavelength will become available through large survey projects and telescopes such as LOFAR<sup>1</sup> (van Haarlem et al. 2013), GMRT<sup>2</sup> (Paciga et al. 2013), PAPER<sup>3</sup> (Ali et al. 2015), CHIME (Bandura et al. 2014), BINGO (Battye et al. 2012, 2013), HERA (Pober et al. 2014), Tianlai (Chen 2012), and SKA<sup>4</sup> (Mellema et al. 2015). Most of these projects aim at measuring signal from the redshifted 21 cm  $\text{H I}$  emission line, from either low-redshift large-scale structure (e.g., Battye et al. 2012; Masui et al. 2013) or high-redshift Epoch of Reionization (e.g., Furlanetto, Oh & Briggs 2006; Paciga et al. 2013). Many of these surveys will suffer from foreground contamination of our own galaxy, the Milky Way, which is typically several orders-of-magnitude larger than the cosmological signals of interest. As a result, a good understanding for this foreground component is crucial

for the interpretation of the cosmological measurements of interest. This need for a deeper understanding of the Milky Way at the relevant  $\text{H I}$  wavelength is the main driver for this work.

To date, only a few of wide-field Galactic maps exist and are available for the community to use to study the  $\text{H I}$  foreground (see de Oliveira-Costa et al. 2008, and reference therein). Furthermore, the frequency coverage has been fairly sparse across the different maps. The most commonly used map around 1 GHz has been the so-called “Haslam map” at 408 MHz (Haslam et al. 1982). This map has been re-processed several times (Remazeilles et al. 2015), but almost no new data has been taken systematically since then. The main reason for the lack of wide-field maps at these frequencies is that historically, this has not been a wavelength window for cosmological measurements. In addition, the generation of these maps require significant observing time even at moderate resolution. With the next generation of  $\text{H I}$  cosmological experiments being built, foreground maps at the radio L-band are becoming more important.

In this work, we investigate the possibility of a simple system that could be used for these foreground maps. This system consists of a dedicated single-dish telescope that scans the sky over several months with very low human intervention during the observation.

<sup>1</sup> <http://www.lofar.org>

<sup>2</sup> <http://www.ncra.tifr.res.in/ncra/gmrt>

<sup>3</sup> <http://eor.berkeley.edu>

<sup>4</sup> <http://www.skatelescope.org>

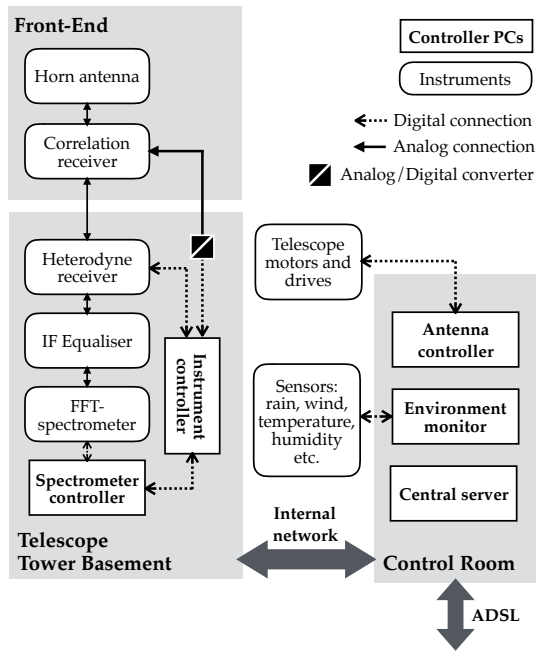


**Figure 1.** Schematic illustration of the entire system for this project. The three grey boxes indicate the three different locations where the instrumentation are – the front-end unit mounted inside the telescope dish, the telescope tower basement, and the control room located about 60 m away from the telescope. The white squares indicate controller PCs whereas the white rounded squares indicate instruments. All computers in the control room connect to each other as well as the external network.

The hardware system is set up at the 7m telescope at the Bleien Observatory, operating in the frequency range 990–1260 MHz. We emphasise the innovative yet low-cost design that resulted in significant improvement in data quality compared to the more conventional systems. This work continues from Chang et al. (2015) as a series of studies at the Bleien Observatory in preparation for future  $H_1$  intensity mapping experiments.

The paper is organized as follows. In §2, we describe our overall system at the Bleien Observatory, both the hardware and the controlling/monitoring mechanism. In §3, we evaluate the performance of the system and the improvement over the previous system with both laboratory measurements and on-sky measurements. Our conclusions are summarized in §4 and additional tests of the hardware system are presented in the Appendix. A companion paper (Akeret et al. in prep, hereafter A16) describes the analysis software and some early processed data.

## 2 SYSTEM DESCRIPTION

In this section, we describe the instrument and software chain from the horn antenna where the signal arrives to the pre-processing step of the data which feeds into the science analysis. Figure 1 shows a schematic illustration of the full system. Table 1 sums up some of the main characteristics of the system, some of which were characterised during the commissioning period.



**Figure 2.** The 7m telescope at the Bleien Observatory and the new feed horn. From this image, one can see the telescope tower, the 7m parabolic dish, and the horn antenna mounted at the focal plane.

### 2.1 The Bleien Observatory

The Bleien Observatory<sup>5</sup> is composed of two parabolic dishes of 5m and 7m diameter and a control room housing supporting instruments. The observatory is located at Bleien, Switzerland, about 50 km south-west of Zurich (geographic latitude  $47^\circ 20' 23''$  north, longitude  $8^\circ 6' 42''$  east, and altitude 469 m). The observatory was built in 1979, which, at the time was a nearly RFI-free location ideal for radio observations. Today, however, the RFI situation is worsened due to the ever-increasing TV and radio stations as well as mobile phone transmitters. Although the site is protected within a 1.5 km via the federal office of communication (OFCOM), significant RFI contamination can still be seen in our data, which is one of the main challenges for the data reduction as we will discuss below.

The 7m dish (F/D 0.507) is used in this work. This telescope is composed of a concrete basement, a steel tower, and an old radar 7 m dish produced during the second World War. Major upgrades during the years of 2002 – 2008 allow more precise pointing and remote control of the telescope. As the original science objective of the telescope has been solar observations, hardware upgrades had to be made to meet the different requirements for cosmological  $H_1$  measurements. The major upgrade on the telescope involves the manufacturing and installation of a new dual-polarization, corrugated horn feed described below. Figure 2 shows the new horn installed at the 7m dish focal plane.

### 2.2 The horn feed

The horn is manufactured by the company ANTERAL in Spain. It is designed to optimally reduce potential side lobes and ground spill-

<sup>5</sup> <http://www.astro.ethz.ch/research/Facilities/Radioteleskop-Bleien>

over. It contains two polarizations with a cross-talk below -24 dB. There is a 4-port ortho-mode transducer in the back of the horn of size 560×560 mm, and the horn itself has a diameter of 450 mm with length 480 mm. The horn weighs 22 kg and has an aperture efficiency  $> 0.6$ . It under-illuminates the dish by a factor of 0.5, which is designed to minimize the side-lobe pickup from the ground and other RFI sources.

### 2.3 The pseudo correlation receiver and the cold reference source

The pseudo correlation receiver (PCR, Mennella et al. 2003) is the core subsystem in the whole chain of the instrument. Its main function is to reduce the  $1/f$ -noise<sup>6</sup> generated in the high-gain, low-noise amplifiers. The term ‘correlation receiver’ refers to the fact that a reference signal is taken together with the sky signal in order to reduce  $1/f$ -noise introduced by the electronics. The term ‘pseudo’ suggests that the correlation operation is implemented via a ‘sum’ operation rather than the more conventional ‘multiplication’ and only requires one analog channel per polarization.

A schematic of the electronic layout of the PCR in our system is shown in Figure 3. Two parallel and almost identical chains are used with one chain connected to the telescope horn receiver at input and the other connected to a cold reference source described below. The signals from both chains are combined to give the “sum” signal at the output of the upper chain, which feeds to the heterodyne receiver described in the next section. The output of the lower chain contains redundant information and is discarded. All components in the PCR are thermally closely linked together and controlled to be at a temperature of  $18.0^\circ \pm 0.2^\circ$ .

In addition to the conventional PCR design, the voltage phase of the PCR in our system can switch between  $0^\circ$  and  $180^\circ$ . Subtracting the received signal from the two phases allows us to further reduce  $1/f$ -noise introduced by the digital backends since the instrumental  $1/f$ -noise from the two electronic chains are not correlated (while the signal from the sky is). In practice, the phase switch is executed every 3 seconds<sup>7</sup>. Phase-switch instruments and other beam-switch or frequency-switch instruments that utilize the same principle have been used frequently in microwave receivers (Kraus 1965; Mennella et al. 2003). However, they are not as often used in radio instruments since the long-term baseline stability has not been a major requirement for traditional radio observations.

The cold reference source is designed to provide a similar spectrum at the same noise level as the science horn to minimize balancing issues in the correlation receiver. Conventionally, such a reference source is either implemented through a separate antenna looking to a dedicated reference sky position, or a resistor cooled with liquid nitrogen. In this work, we demonstrate a low-cost alternative of using an electronic source, based on commercially available components: the reference source is composed of an inversely connected

low-noise amplifier and a broad-band ferrite isolator. The additional advantage of an electronic reference is that it does not generate undesired interference with the environment and the science signal. The basic principles behind this design was first developed in (Frater & Williams 1981), but so far there are only few existing implementations shown in Fabry & Meunier (2009); Straub, Murk & Kämpfer (2010); Scheeler & Popovic (2013).

The remaining elements in the electronic chain shown in Figure 3 are tested in the lab as well as in simulations to achieve the ultimate high-gain, low-noise required between the antenna and the rest of the chain. We also note that the band-pass filter (BPF) is applied at the end of the electronic chain to narrow down the frequency range to close to our final target.

### 2.4 The heterodyne receiver

The heterodyne receiver (HRX) is introduced to resolve the mismatch between the frequency range of our expected signal (990–1260 MHz) and the frequency range where the FFT-spectrometer operates (below 800 MHz). The HRX down-converts the frequency range of the incoming signals using a local oscillator and a mixer circuit. In addition, the HRX provides a gain of  $\sim 40$  dB, which is needed to drive the analog digital converter of the FFT-spectrometer. The HRX also includes a high-pass filter which suppresses radiation from nearby mobile phone transmitters at  $\sim 950$  MHz and a low-pass filter to avoid aliasing in the FFT-spectrometer<sup>8</sup>. The HRX is physically part of the instrument controller to keep cabling short and temperature as constant as possible. A schematic diagram of the electronic layout of the HRX is shown in Figure 4.

### 2.5 The FFT-spectrometer

The FFT-spectrometer receives the analog signals output from the HRX after the equalizer<sup>9</sup>. The signal is first digitized and then processed in a Field Programmable Gate Array (FPGA) unit. A schematic of the FPGA unit is shown in Figure 5. The spectral analysis is based on FFT on a  $32k \times 32k$  grid, which in our setting results in a frequency channel separation of 48.8 kHz. The main improvement of this FFT-spectrometer over older implementations (Benz et al. 2005) is its digital filterbank, which convolves the input signal with a chosen filter to better separate the channels and reduce side-lobe contamination. The built-in filterbank of our FFT-spectrometer includes different windowing functions such as Hamming, Hanning, Blackman-Harris, and Flattop. Based on simulations and laboratory tests, we find that the Flattop window function results in the best performance in our case. The FFT-spectrometer also has a high dynamic range of 70dB, which implies that the high-level RFI is less likely to saturate and leak into neighbouring bands. Although not used directly in our main analysis, the filterbank core has several other powerful functionalities: computing sum and difference of the spectra, sideband separation, cross power spectrum, and recording square of the power spectrum for kurtosis analysis (Nita & Gary 2010).

<sup>8</sup> The bandwidth of the signal has to be limited to half the sampling frequency which in our case is 1600 MHz.

<sup>9</sup> Due to the 25m-long coaxial cables between the PCR and the HRX, there is a large spectral slope in the order of 10dB in our frequency range, which is unideal in terms of the dynamic range of the spectrometer. The spectrum equalizer is added to attenuate lower frequencies more than higher frequencies, resulting in a flat final spectrum.

<sup>6</sup>  $1/f$ -noise refers to the noise component which has a power spectrum that scales with inverse frequency. This means that the noise is more correlated over long time-scales and less correlated over short time-scales.  $1/f$ -noise is typically generated in all electronic devices.

<sup>7</sup> The choice of this integration time has been originally chosen to minimize the fraction of deadtime between integrations. In the current system, this deadtime is no longer a problem, but we keep the integration time as the gain in going to shorter integration time is not significant. This also gives a reasonable data volume ( $\sim 17$ MB per 15 minutes) to handle in the later analyses.

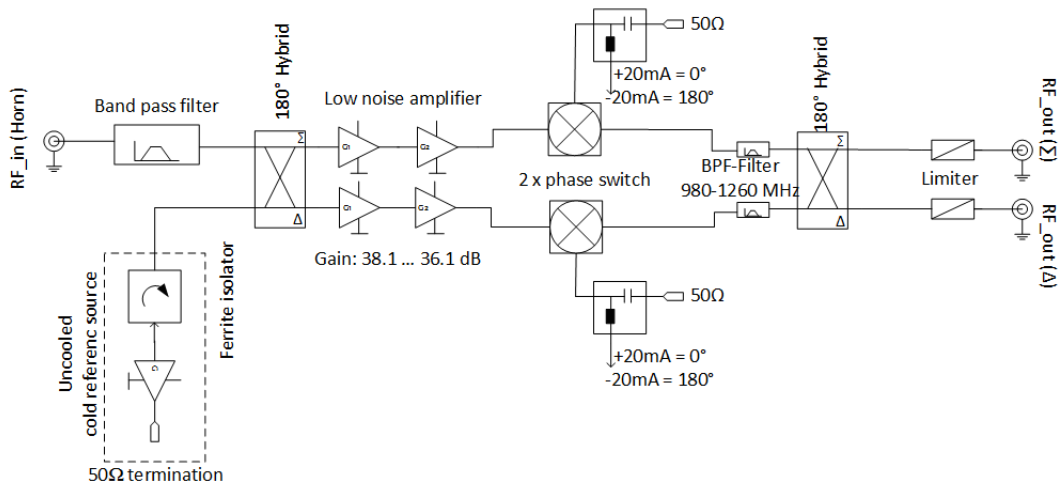


**Figure 3.** Schematic diagram of the PCR. Two parallel and almost identical chains are shown, with the electronic signal propagating from left to right. The upper chain is connected to the telescope horn receiver on the left and the lower chain connected to the cold reference source as labeled. The final output of upper chain contains is fed to the heterodyne receiver (§2.4), while the lower chain is not used.

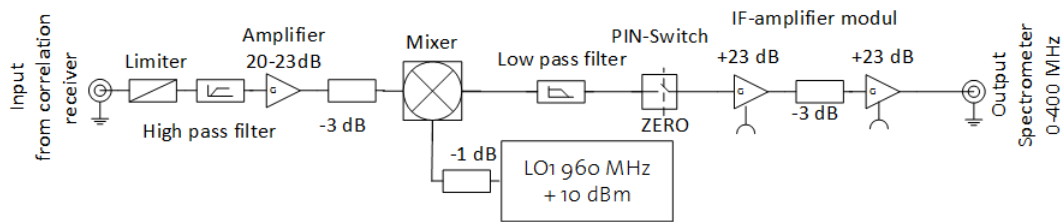


**Figure 4.** Schematic diagram of the HRX.

As discussed in §2.3, we operate the PCR in phase-switch mode. In the default setting of the FFT-spectrometer, this means that a file is written every time the phase-switch happens, i.e. every  $\sim 3$  seconds. This is not ideal since it generates a large number of single-spectrum files and some latency dead-time in the communication between the FFT-spectrometer and the PCR especially in the early stage of the experiment. Nevertheless, given the data taken, we describe in §2.7 how we process the data into more user-friendly formats. Future models of this FFT-spectrometer will improve on this feature.

## 2.6 Instrument control and monitoring

The full system is controlled via several control PCs inside the telescope tower and the control room. The five main PCs are marked as rectangles in Figure 1. They communicate with the antenna, the PCR, the HRX, the FFT-spectrometer and other monitoring sensors around the observatory. The interfaces are based on the ARDUINO UNO micro-controller<sup>10</sup>. There is no digital communication between the controller computer and the front-end (including the horn antenna and the PCR) to avoid self-produced interference. All information from and to the front-end is fed with analog wiring.

The antenna controller PC is connected to the 7m dish antenna

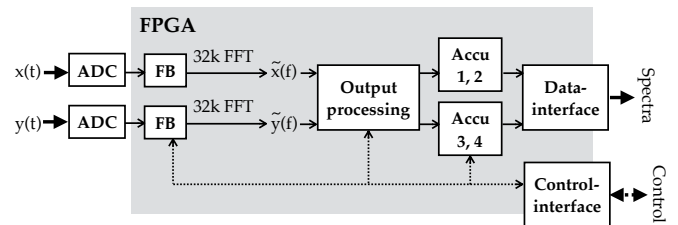


**Figure 5.** Schematic diagram of the FPGA unit in the FFT-spectrometer.  $x(t)$  and  $y(t)$  are the signal from the two polarizations (which we only use one in our case). The analog-to-digital converter (ADC) digitalizes the signal before entering the FPGA unit. After a Fast Fourier Transform (FFT), the signal is processed and accumulated via the accumulator (Accu) for both the spectral power density (P) and the variance of P. We control the FPGA via the control-interface and access the final spectral data output via the data-interface.

via a commercial dual drive system (one axis for the azimuth direction and a second axis for the elevation direction). It is also linked to the internal network and to the Internet for remote access. The main functions of this controller PC is to send commands related to the pointing position of the telescope. This includes fixed celestial positions, tracking of astronomical sources, and specific scanning patterns for special calibration purposes (e.g. 2D raster-scans for pointing calibration). A pre-designed survey schedule can be provided

<sup>10</sup> <https://www.arduino.cc/en/Main/ArduinoBoardUno>

to automate long observation plans. The control system records the time and position of the telescope, which is measured by optical encoders, directly mounted to the axis of the telescope. The positioning resolution is given by the number bits. In our case, 12 bits leads to a pointing resolution of  $0.088^\circ$ .

The instrument controller PC communicates with the PCR and the HRX via USB. The main tasks of this PC include commanding the phase switch to the PCR and regulating the temperature of the high-frequency components in the focal plane unit. Large changes in temperature are regulated by a 2-point regulator to heat/cool with Peltier elements, while small temperature changes are controlled via Proportional plus Integral plus Derivative (PID) elements. Measurement of the ambient temperature, electronics temperature, humidity and the voltage supply of the different parts are sent back to the controller computer and recorded for real-time monitoring. It also connects to the spectrometer controller PC that controls the FFT-spectrometer.

The environment monitor PC is connected to the internal network and collects information from the different environmental sensors in and around the observatory, including wind, rain, temperature and humidity. And finally, the central server serves as a dedicated data server and stores all the raw spectral, environmental and instrumental data. It also serves as the web server for the monitoring website. A real-time internal monitoring website is set up for easy monitoring of all the data collection and instrument/environment status.

## 2.7 Data pre-processing

As mentioned in §2.5, the FFT-spectrometer writes out one file per measurement for every integration period. In the current setup the system measures a spectral power density ( $P$ ) and its variance ( $P^2$ ) in both voltage phases. The accumulation period is defined to be  $146484$  (number of samples)  $\times$   $20.48\mu\text{sec}$  (sampling time)  $\approx 3.0$  sec. In a continuous operation of several weeks, the number of created files rapidly exceeds the capabilities of regular file systems. To circumvent this an independent process collects and aggregates the single spectrum files in a fixed interval (currently set to be 15 minutes). Additionally, a ‘time axis’ is created that hold information about the time when each spectrum was measured. During this aggregation process, frequency channels which are outside the band-pass filter are discarded to reduce the data volume. Finally, the aggregated data is written to disk in HDF5 file format and a moderate, lossless gzip compression is applied. By discarding obsolete data and the file compression the data volume is reduced by a factor 3.5 on average. See A16 for a detailed description of the data structure.

## 3 COMMISSIONING

A two-stage commissioning process was carried out from mid-November to mid-December of 2015. The first stage involves testing the new hardware in the laboratory, while the second stage includes installing the system at the observatory and performing on-sky measurements. Results from the two stages are presented below.

For the purpose of illustration, in the following we often compare the performance of our new phase-switch correlation system with another system that does not include some of these major improvements described in §2. A convenient choice for this system is the data collected through the other polarization of the horn feed. This data will come from exactly the same part of the sky and be

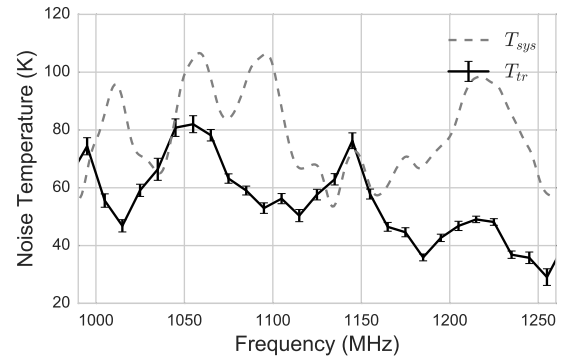


**Figure 6.** Mean and uncertainty of the noise temperature of the PCR ( $T_{rx}$ ) measured over 10 MHz bins in the frequency range of interest. The black solid line is the average  $T_{rx}$  and the grey dashed line shows the total system noise temperature  $T_{sys}$ .

contaminate by almost the same RFI signals. The signal is then connected to an electronic chain that does not have the PCR and phase-switch implementation, and eventually to an identical FFT-spectrometer. Effectively, this comparison shows the improvement of our new design over a more conventional radio telescope system. When applicable, we refer to this other system as the ‘total-power chain’, as there is no phase-switch operation in this chain. The schematic layout of the total-power chain would be very similar to Figure 1, except that it does not contain the correlation receiver.

In Appendix B, we present several additional tests that are not directly associated with the new electronic system described earlier, but are generally important in terms of the planning of a Galactic survey. These tests include the site RFI characterization, the telescope pointing accuracy, the beam size, gain and system temperature. The tests were performed both during the commissioning period and the ‘Science Verification’ stage that followed shortly after commissioning (see Appendix A for a brief description of the Science Verification observations).

### 3.1 Laboratory measurements

Measurements in the laboratory were performed to test the entire electronic chain from the PCR to the recording of the FFT-spectrometer. The main focus at this stage is to test for the noise temperature of the PCR ( $T_{rx}$ ) and the  $1/f$ -noise from the electronic chain.

The PCR is expected to be the main contributing factor to the total noise temperature. As a result, an important laboratory measurement is the quantification of the noise temperature of the PCR when decoupled from the rest of the system (the sky, the horn, the cabling and the network). We perform the measurement by comparing the PCR recording under the known ambient temperature and liquid nitrogen temperature ( $\sim 78$  K). Figure 6 shows the mean receiver noise temperature of the PCR over the full frequency range. We note that this noise temperature is a significant improvement over the total-power chain, which is about 200 K. This improvement mainly comes from the cancellation of  $1/f$ -noise from both the PCR and the phase-switch implementation. We also overlay in Figure 6 the noise temperature measured for the entire system including the sky measured at the telescope, or the system temperature  $T_{sys}$  (see Appendix A for the calculation of  $T_{sys}$ ). We note that the  $T_{sys}$  is very

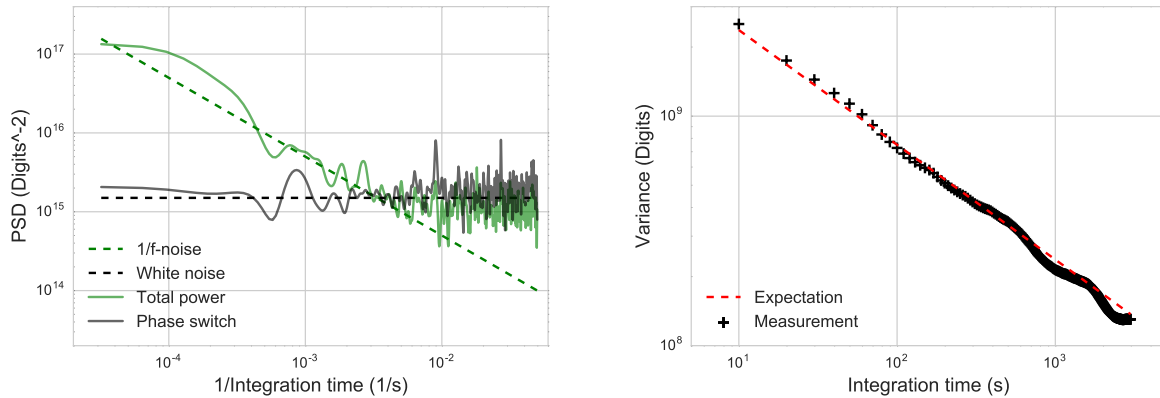


**Figure 7.** PSD measurement from the FFT-spectrometer in total-power and phase-switch modes (left), and the corresponding Allan time variance measurement for the phase-switch mode (right). The left panel is smoothed by a Gaussian filter with standard deviation of 3 Hz. It illustrates how the phase-switch implementation effectively reduces the  $1/f$ -noise in the data. The right panel shows that the Allan time variance measurement confirms that the noise does average down as inverse integration time.

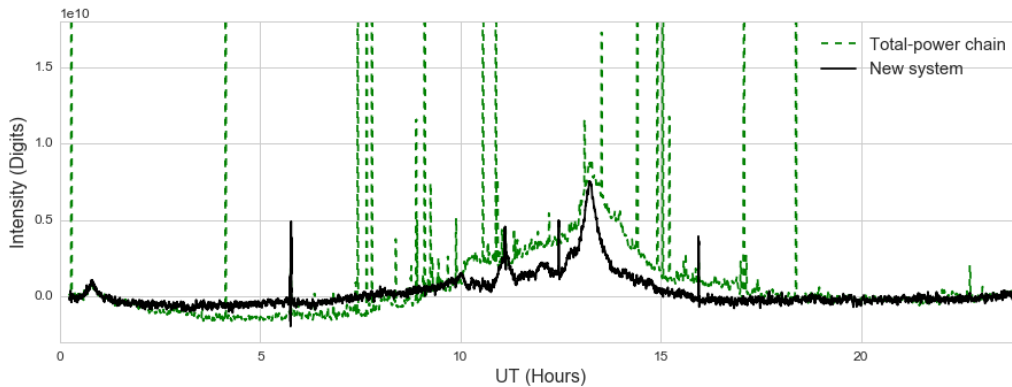


**Figure 8.** Drift-scan data for one day at  $\sim 1008$  MHz. Data from the total-power chain (dashed green) is overlaid with data from the new system (solid black) for comparison. Both data have been smoothed over 10 pixels ( $\sim 1$  minute) and the median level over the whole day has been subtracted. One can clearly see a less stable baseline in the total-power chain. The RFI level is also higher in the total-power chain, which is mainly due to the fewer filters in the chain.

close to  $T_{rx}$ , and the difference is consistent with the temperature of the background sky. This demonstrates that other sources of noise in our system are small. Note that there are also potential errors due to the inaccuracy in the ambient temperature measurement and the liquid nitrogen temperature.

To measure the  $1/f$ -noise in our laboratory data, we first look at the power spectrum density, or PSD, of the data. The PSD for each frequency channel is calculated by taking the Fourier transform of the time-sequenced data. The PSD measured in the laboratory gives a measure of the instrument  $1/f$ -noise – pure white noise will have a flat power spectrum while pure  $1/f$  (pink) noise will show a power spectrum with a slope of  $-1$  when plotting on a log-log scale. As both the PCR and the phase-switch implementation of the system are designed to reduce the  $1/f$ -noise, it is important to verify that the  $1/f$ -noise is indeed under control. The left panel of Figure 7 shows the power spectrum from a single frequency channel in the FFT-spectrometer with and without implementing the phase-switch operation. We see that the  $1/f$ -noise is greatly reduced when operating in the phase-switch mode. This also demonstrates that with

the PCR alone, we still have significant  $1/f$ -noise in the data. Another way to examine the residual  $1/f$ -noise in the data is to calculate the Allan time variance as a function of integration time (Allan 1966). In the case of pure white noise, the Allan time variance is inversely proportional to the integration time. Here we follow the measurement technique proposed by Ossenkopf (2008) and derive the Allan time variance curve of our system. The right panel of Figure 7 shows the result of this measurement for a single frequency in phase-switch mode, where we recorded data for 18 hours. The plot shows clearly that the final Allan time variance of our electronic chain follows nicely the expectation for a white-noise system. This again suggests that the instrument is stable on time scales of at least tens of hours.

### 3.2 On-site measurements

The full electronic chain was installed at Bleien on November 10, 2015 and the full system began operation soon after. The on-sky commission period continued till December 14, 2015, during which

**Table 1.** Instrument specifications.

Instrument parameter	Value and unit
Observatory location	Graenichen, Switzerland 47° 20′ 23″ N, 8° 6′ 42″ E
Observatory altitude	469 m
Telescope geometry	7 m parabolic dish
Telescope mount limits	45° < Az < 315° 5.4° < Ele < 87°
Frequency range full sensitivity	990 MHz - 1260 MHz
Frequency range reduced sensitivity	970 MHz - 1360 MHz
Receiver temperature	≤ 80 K
Allan-time	≥ 5000 s
Channel separation	48.8 KHz
Radiometric bandwidth	51.5 KHz
Integration time per phase	3 s
ADC resolution	12 bits
# of channels in spectrometer	16584
ADC clock rate	1600 MHz
ADC input voltage	2 V maximum at 50Ω
Temperature control receivers	Tambient -8 K, +18 K
Cold reference noise	40 K ± 10 K
Dynamic range	≈ 70 dB
Power consumption per antenna	110 W
Maximum rf input power	-70 dBm

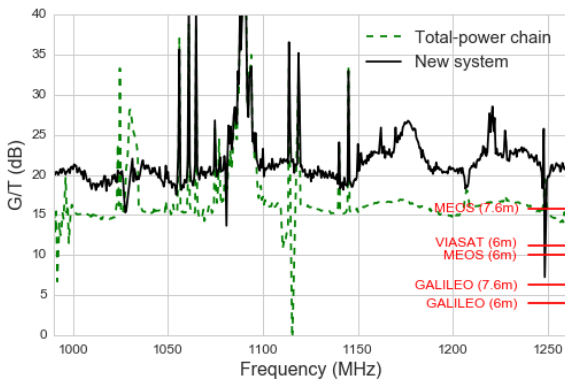


**Figure 9.**  $G/T$ -factor calculated using Cassiopeia A, for the total-power chain (dashed green) and the new system (solid black). The large peak at 1080 MHz is an artefact from the high-level emissions of the Automatic Dependent Surveillance radars and altimeters. Also overlaid are some average  $G/T$ -factors for other dishes of similar size.

we performed various tests to examine and tune the performance of the new system. A set of general calibration tests during this period and in the following SV stage are described in Appendix A. Here we only present the qualitative comparison between the new system and the total-power chain to demonstrate the improvement in the data quality from the new innovative hardware design.

Figure 8 shows the time-sequenced data for the mean of 20 frequency channels around 1008 MHz for a characteristic day for both the total-power chain and the new system. The data plots shown have been median-subtracted and scaled to have the same signal strength for easy comparison. The telescope is parked at position  $Az=200.0^\circ$  and  $Ele=46.0^\circ$  at this date, which corresponds to mapping the sky at  $DEC=4.9^\circ$ . The telescope beam drifts through the Milky Way at

~ 13.5 UT, which can be seen clearly on the plot. Both data sets are smoothed with a top-hat filter of 50 pixels. From the plot, we find that the baseline drift in the new system is much reduced compared to the total-power chain. We also see that this stability comes at the price of a higher noise level. We note that there are also 3 additional high- and low-pass filters in the new system compared to the total-power chain, which is the main reason for reduced RFI contamination in the new system.

A useful measure of the instrumental performance is the “ $G/T$ -factor” (Baars et al. 1977; Kildal, Skyttemyr & Kishk 1997) defined through

$$\frac{G}{T} = \frac{8k\pi(Y-1)}{S\lambda^2} \quad (1)$$

where  $k$  is the Boltzmann constant,  $Y$  is the Y-factor<sup>11</sup> for a source with known flux  $S$ , and  $\lambda$  is the wavelength of interest. For a given source and wavelength, the  $G/T$ -factor scales like  $Y-1$ , which is the ratio of the signal to the background. The advantage of using this figure-of-merit is that it does not depend on the measurement of beam size, system temperature and other method-dependent procedures. The only data required is a transit measurement of a known source. For dishes of the same size, the  $G/T$ -factor is a measure of the performance of an instrument. Figure 9 shows the  $G/T$ -factor calculated for the total-power chain and for the new system. We find that the design of the new system effectively increases the  $G/T$ -factor by more than 5dB  $\approx 316\%$  in almost all frequencies. This again demonstrates the power of the PCR and the phase-switch implementation. We also overlay the  $G/T$ -factors for several other radio telescopes<sup>12</sup> with dishes of similar sizes to show that the performance of our instrument is above average amongst similar-class telescopes.

## 4 CONCLUSION

In this paper we describe the design of an integrated system at the Bleien Observatory for mapping the Galaxy. The system is designed to map the Milky Way in the L-band frequency range 990–1260 MHz with a 7m single-dish telescope. The ultimate science goal of this system is to provide a set of new data for studying the foreground effect of future low-redshift  $H_I$  intensity mapping cosmology experiments such as BINGO and HIRAX. Specifically, the data from this system will fill the gap between the Haslam map at 408 MHz and the various maps constructed at the 21 cm frequency (1420 MHz). This data will also allow for explorations in different areas of Galactic astronomy. We describe the hardware upgrade of the 7m single-dish telescope at the Bleien Observatory from a more conventional electronic chain to a high-performance, stable system. We also demonstrate that the improvement in the data quality is significant.

Several innovative designs in the hardware system result in a very stable system (Allan-time > 5000 s) with high dynamic range (70 dB) and high frequency resolution (50 kHz), which is important for the large-scale Galactic map. These innovations include the

<sup>11</sup> The Y-factor is a measure of the ratio of the signal+background and the background and is commonly used in radio astronomy. It is defined as the ratio of the flux at the center of the source over the background.

<sup>12</sup> These  $G/T$  values are taken from the International Telecommunication Union (ITU) report Rec. ITU-R S.733-2: “Determination of the  $G/T$  Ratio for Earth Stations Operating in the Fixed Satellite Service”.

pseudo correlation receiver and the cold reference source within the receiver, the FFT-spectrometer and the phase-switch operation of the whole system. Some of these components have been well tested and developed in the microwave instruments for cosmic microwave background (CMB) measurements, but for radio astronomy, these technologies driven by large-scale cosmology are relatively new. The hardware system presented in this work provides an environment to test many of these new ideas for a radio telescope.

The hardware system described in this paper together with the software pipeline developed in the companion paper A16 can be fed into the planning of a generic Galactic mapping survey. Future potential upgrades of this system include building a parallel electronic chain for the second polarization, installing ground-shields to reduce ground-pickup and RFI, and making the FFT-spectrometer more programmable so that more powerful functionalities in the spectrometer can be used. One interesting extension is to use the internal correlation function in the FFT-spectrometer to replace the front end correlation receiver (Kooi et al. 2004). This potentially could save hardware cost significantly.

#### ACKNOWLEDGEMENT

We thank apprentice Manuela Wipf for manufacturing the phase switched pseudo correlation receiver, the heterodyne receiver and the instrument controller. We also thank the mechanical workshop of ETH for production of dozens of mechanical parts for the receiver chain. We thank farmer Andreas Brunner and Marc Furrer from Electricity Power Supply Gränichen for technical support with their hydraulic lifting ramp during installation of the heavy corrugated horn-antenna.

#### REFERENCES

- Ali Z. S. et al., 2015, *ApJ*, 809, 61  
 Allan D. W., 1966, *IEEE Proceedings*, 54  
 Baars J. W. M., Genzel R., Pauliny-Toth I. I. K., Witzel A., 1977, *A&A*, 61, 99  
 Bandura K. et al., 2014, in *SPIE*, Vol. 9145, Ground-based and Airborne Telescopes V, p. 914522  
 Battye R. A. et al., 2012, *ArXiv e-prints*  
 Battye R. A., Browne I. W. A., Dickinson C., Heron G., Maffei B., Poursidou A., 2013, *MNRAS*, 434, 1239  
 Benz A. O., Grigis P. C., Hungerbühler V., Meyer H., Monstein C., Stuber B., Zardet D., 2005, *A&A*, 442, 767  
 Briggs F. H., Sorar E., Kraan-Korteweg R. C., van Driel W., 1997, *PASA*, 14, 37  
 Chang C., Monstein C., Refregier A., Amara A., Glauser A., Casura S., 2015, *PASP*, 127, 1131  
 Chen X., 2012, *International Journal of Modern Physics Conference Series*, 12, 256  
 de Oliveira-Costa A., Tegmark M., Gaensler B. M., Jonas J., Landecker T. L., Reich P., 2008, *MNRAS*, 388, 247  
 Fabry F., Meunier V., 2009, in *8th International Symposium on Tropospheric Profiling, S06-P03-1*, Delft, NL  
 Frater R. H., Williams D. R., 1981, *IEEE Transactions on Microwave Theory Techniques*, 29, 344  
 Furlanetto S. R., Oh S. P., Briggs F. H., 2006, *Physics Reports*, 433, 181  
 Haslam C. G. T., Salter C. J., Stoffel H., Wilson W. E., 1982, *A&AS*, 47, 1

- Kildal P.-S., Skyttemyr S. A., Kishk A. A., 1997, *IEEE Transactions on Antennas and Propagation*, 45, 1130  
 Kooi J. W. et al., 2004, in *SPIE*, Vol. 5498, Z-Spec: a broadband millimeter-wave grating spectrometer: design, construction, and first cryogenic measurements, Bradford C. M., Ade P. A. R., Aguirre J. E., Bock J. J., Dragovan M., Duband L., Earle L., Glenn J., Matsuhara H., Naylor B. J., Nguyen H. T., Yun M., Zmuidzinas J., eds., pp. 332–348  
 Kraus J., 1965, *Radio Astronomy*. Quasar Books Company, New York  
 Masui K. W. et al., 2013, *ApJ*, 763, L20  
 Mellema G., Koopmans L., Shukla H., Datta K. K., Mesinger A., Majumdar S., 2015, *Advancing Astrophysics with the Square Kilometre Array (AASKA14)*, 10  
 Mennella A., Bersanelli M., Seiffert M., Kettle D., Roddis N., Wilkinson A., Meinhold P., 2003, *A&A*, 410, 1089  
 Nita G. M., Gary D. E., 2010, *MNRAS*, 406, L60  
 Ossenkopf V., 2008, *A&A*, 479, 915  
 Paciga G. et al., 2013, *MNRAS*, 433, 639  
 Pober J. C. et al., 2014, *ApJ*, 782, 66  
 Popping A., Braun R., 2008, *A&A*, 479, 903  
 Remazeilles M., Dickinson C., Banday A. J., Bigot-Sazy M.-A., Ghosh T., 2015, *MNRAS*, 451, 4311  
 Scheeler R., Popovic Z., 2013, in *Compound Semiconductor Integrated Circuit Symposium (CSICS)*, 2013 IEEE, pp. 1–4  
 Straub C., Murk A., Kämpfer N., 2010, *Atmospheric Measurement Techniques*, 3, 1271  
 van Haarlem M. P. et al., 2013, *A&A*, 556, A2

#### APPENDIX A: SCIENCE VERIFICATION

The Science Verification (SV) period took part from mid December 2015 to end of May, 2016 after commissioning. During the SV, observations were carried out to mimic a real survey in terms of the survey strategy and scheduling.

Based on analyses of data from commissioning considerations of resolution, total coverage, signal-to-noise, calibration and turnaround, the scanning strategy for SV is composed of the following elements:

- Each 16-day periods is composed of 2 “calibration days” and 14 “survey days”. The calibration days are planned in the beginning and the middle of the season. This pattern is used for the entire survey.
- The first part of the survey consists of seven 16-day periods, where 5 are done at  $Az=200^\circ$  to fill in the south part of the sky, and the other two seasons are done at  $Az=280^\circ$  and  $Az=314^\circ$  to fill in the north part of the map.
- The map from the data described above is then used for planning the second part of the survey, where the largest masked positions are re-observed. This second part took about 1 month.

Data was taken to mimic a large-scale Galactic survey, resulting in a final sky coverage of  $\sim 29,393 \text{ deg}^2$  in the region  $-33^\circ < \text{Dec} < 60^\circ$ . The SV observations included 139 survey days and 21 calibration days. The data was analyzed using the software developed in A16, and some preliminary are also shown therein.



**APPENDIX B: ADDITIONAL TESTS ON THE OVERALL SYSTEM**

In this appendix we present a series of tests on the hardware system. These tests are important for the planning of a generic Galactic survey. All tests were performed during commissioning and the SV period.

**B1 Site RFI characterisation**

As mentioned in §2.1, one major challenges for our system is the RFI contamination at the Bleien Observatory. In addition to the site conditions, the frequency range of our instrument sits in the L-band (1-2 GHz) where many commercial, navigation, and surveillance applications lie. Figure B1 shows one example of the raw time-frequency plane data from the FFT spectrometer and the most pronounced RFI sources. In order to understand the frequency range and potential locations of strong RFI emission sources, we perform three 2D terrestrial scans within the range of positions accessible by the telescope.

All three scans were performed in identical patterns. Each scan moves through the positions  $47^\circ < Az < 313^\circ$  for 32 elevation angles equally spaced in the range  $6^\circ < Ele < 86^\circ$ . The limits are imposed by the limits that the telescope can physically point to due to trees on the site, while the elevation interval is chosen to be just smaller than the beam size. Each horizontal scan takes  $\sim 20$  minutes.

Figure B2 shows examples of the resulting terrestrial map generated from the data for the two frequency channels in the three scans. The plots are in terrestrial coordinates, Azimuth (Az) and Elevation (Ele), and are shown without spherical projection. The black line traces out the horizon from the mountains surrounding the area, which can be seen to emit thermal radiation much higher than the sky. Two regions of additional emission beyond the black line at  $Az=85^\circ$  and  $265^\circ$  are known manmade structures (the control room of the telescope and the farmer’s house). The yellow line traces the geo-stationary path, where there is a much higher chance of seeing strong point source emissions from the satellites. We note that the trajectories of other types of satellites on these plots will be more complicated.

The left panels show a relatively clean frequency channel, where only few RFI pixels are seen. The galaxy can be seen clearly as a stripe across (from  $Az=115^\circ$  at  $Ele=10^\circ$  to  $Az=250^\circ$  at  $Ele=75^\circ$  for the first two scans and from  $Az=240^\circ$  at  $Ele=10^\circ$  to  $Az=300^\circ$  at  $Ele=40^\circ$  for the last scan), and there is smooth background gradient coming from the hot horizon leaking into the side- and back-lobe of the telescope. We also note that the baseline is not the same for all three days. The right panels show the maps at a frequency channel where there is strong RFI emission everywhere, channels like these are in general not usable, as the resulting maps will be heavily masked.

Comparing maps from the same frequency channel across days, we observe that for the clean channel, (1) the position of the galaxy shifts over time (2) geostationary satellites do not change positions and (3) there are a few more point-like sources in the maps, which would be other types of satellites as the positions are not exactly the same in the two maps. For the contaminated channel, on the other hand, the emissions are scattered randomly across the field aside from the geostationary satellites.

These RFI maps help us to ensure that the drift-scan positions do not point into known high RFI regions during the scans. It also gives us a qualitative understanding of the RFI environment in the area. We find that within our frequency range of interest, there are

a few localized clean frequency bands at the low frequency end and around 1180 MHz, but most other frequencies outside these bands are contaminated by RFI at a median to serious level. This again manifests the challenge in observing in L-band, where the cell phone (925–960 MHz<sup>13</sup>), aircraft navigation (1025–1150 MHz), and GPS satellite (1176 MHz, 1228 MHz) communication bands lie, and also highlights the importance of a good RFI mitigation algorithm.

**B2 Pointing calibration**

A general Galactic map needs to be built based on knowing where the telescope is pointing. Thus it is important to understand the uncertainty in the pointing of the telescope, or, the difference between the recorded telescope pointing coordinates and the actual pointing coordinates. We performing 2D raster scans of the Sun, a bright source whose position on the sky we know accurately. As we do not expect this uncertainty to change dramatically over time, we only perform two measurements before and during the survey. Also, since the FFT spectrometer does not have a sufficiently fine time resolution, we use another instrument (the Callisto spectrometer) to perform this measurement. The Callisto spectrometer is connected to the same horn antenna as the FFT spectrometer, but using a different electronic chain. This, however, should not affect the validity of the pointing measurement.

We plot the scanned result on the coordinates according to the telescope recording, where the center is where we expect the Sun to be. If the pointing of the telescope was perfect, we would expect the center of the Sun to be measured at (0,0) in these coordinates. For the 3 measurements that was made, we find the mean and  $1\sigma$  uncertainty on the mean for the pointing errors over all frequencies to be  $4.17 \pm 0.15$  arcmin ( $-1.56 \pm 1.41$  in Az direction,  $-3.87 \pm 1.68$  in Ele direction)  $11.56 \pm 0.21$  arcmin ( $-11.56 \pm 1.60$  in Az direction,  $-0.32 \pm 2.57$  in Ele direction) and  $11.42 \pm 0.20$  arcmin ( $-11.38 \pm 1.74$  in Az direction,  $0.97 \pm 2.26$  in Ele direction).

We note that two other effects need to be considered when interpreting the results. First, the telescope is constantly moving in the Az direction when performing these 2D scans, meaning that when the telescope is moving fast, the pointing in that direction will less accurate compared the other direction, and also less accurate compared to when the telescope is static (i.e. in a drift-scan mode). We indeed see this trend in the data. For the latter two measurements, the scanning velocity was much faster than the first one, and we see there is a much larger error in the Az direction. Second, there is an inherent inaccuracy in the telescope recording coming from the fact that it only records every  $\sim 7$  seconds. In a drift-scan scenario, this means that the pointing cannot be known better than  $\sim 5$  arcminutes, which is larger than the static pointing error we can infer from the Ele direction measurement discussed above, and the Az direction in the first measurement.

To summarize, we expect the pointing error in our data during the entire survey to be limited by the telescope recording at  $\sim 5$  arcminutes.

<sup>13</sup> Although this frequency range is not directly in our band, the very strong signal can saturate and leak into our band if the filters were not properly installed.

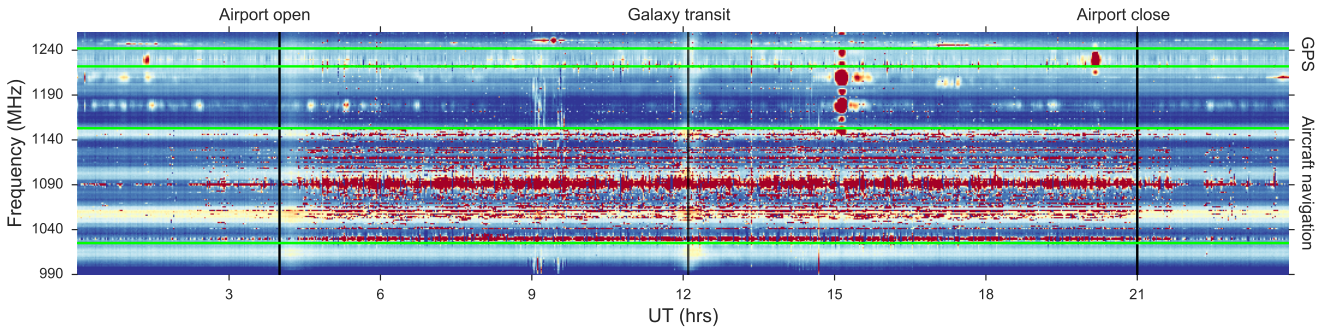


**Figure B1.** Example of the raw time-frequency plane from the FFT spectrometer taken on May 10, 2016. Specific bands in time and frequency are marked to show the most pronounced RFI sources, including the aircraft navigation band and the GPS satellite band. Also marked is the expected crossing of the galaxy.

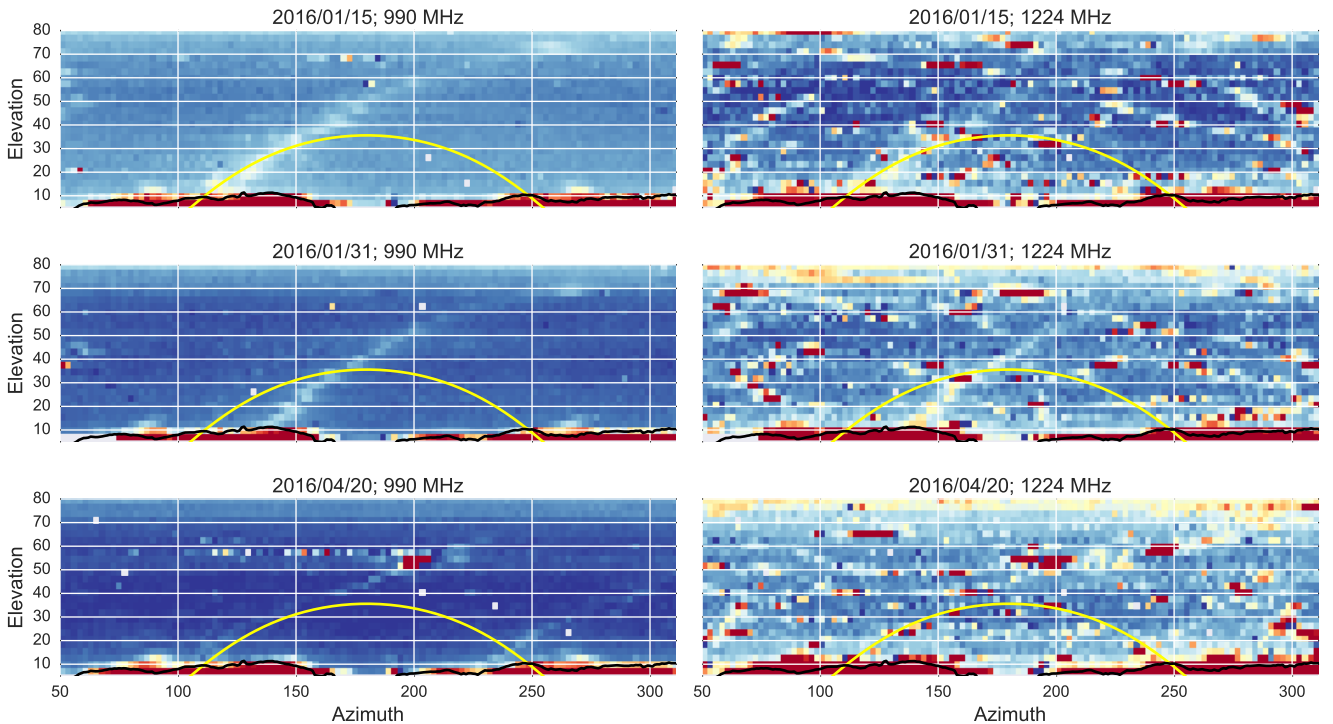


**Figure B2.** Terrestrial scan of the observable region for the 7m dish at the Bleien Observatory for three different days (January 15, January 31 and April 20 of 2016 from top to bottom). The left panels show the maps for a relatively clean channel (990 MHz), whereas the right panel is more contaminated by RFI (1224 MHz). The color scale is the same for panels of the same frequency channel. The color scales for the left and the right panels span the same range, but adjusted so that the background levels are similar for easy visualization.

### B3 Beam size

The most important aspects of the beam is the beam size, as it directly determines the limiting resolution of the telescope. We measure the beam size using 1D transit measurements of the Sun, as it provides high signal-to-noise for the measurement. For our telescope beam ( $\sim 2.7^\circ$  FWHM), the Sun is nearly a point source ( $\sim 0.63^\circ$  FWHM). Nevertheless we subtract a fixed size of the Sun in quadrature when quoting the measured size of the beam. We monitor the beam size throughout the entire Science Verification period.

12 out of the 21 calibration days contain Sun measurements,

and 2–4 measurements were made each day. We first fit a Gaussian profile to each transit measurement in each frequency channel and calculate the resulting FWHM of the profile as a function of frequency as shown in the left panel of Figure B3. The cleaned, median measurement and the beam size after removing the Sun contribution is overlaid in the figure together with the expected beam size for an idealized 7m dish. We observe several features in these results. First, on top of the expected  $1.22\lambda/D$  trend, there are so-called “standing-wave” features in the beam size measurements. This is similar to that reported in Briggs et al. (1997); Popping & Braun (2008); Chang et al. (2015), and is caused by the physical standing waves generated

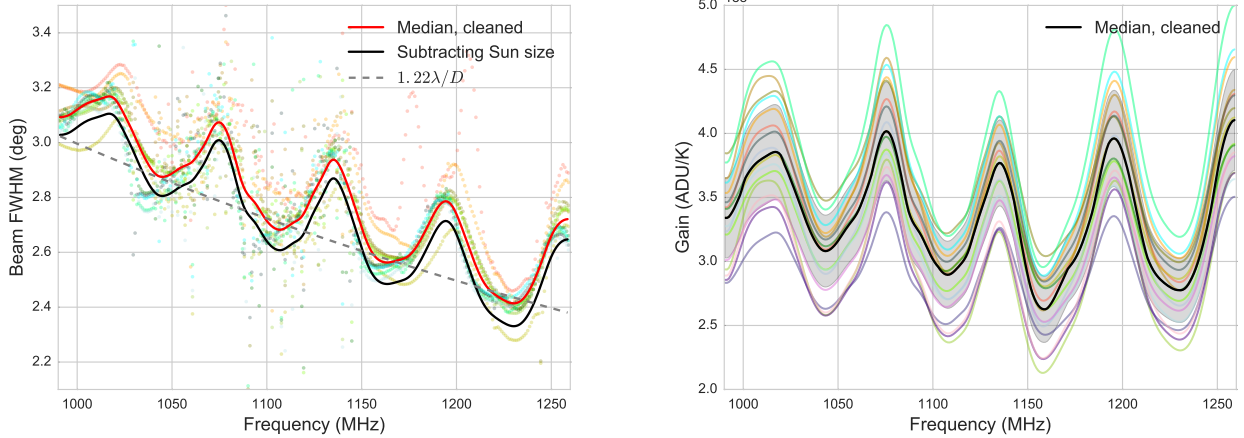


**Figure B3.** Left: beam size measured using the Sun as a function of frequency. The data points of different colors show the measurement performed on different days distributed over the Science Verification period, while the median, cleaned beam size measurement is shown in red. Subtracting the Sun size in quadrature gives the black line, which is our final beam size. Right: the gain calibration results measured from Cassiopeia A as a function of frequency is shown. Different colors represent measurements performed on different days. The grey shaded region shows the standard deviation over all the curves.

from the interference of the electromagnetic wave reflecting between the front end and the dish, as well as in the electronics. Second, the measurements are significantly noisier in the frequency range 1025–1150 MHz due to RFI contamination. Finally, there appears to be a  $\sim 10\%$  variation in the measured beam size over time. This can be due to the size variation of the observed Sun and the change in beam size over elevation.

#### B4 Gain calibration and system temperature

We demonstrate the flux calibration of our system based on Cassiopeia A, as its spectra is well-understood (e.g., Baars et al. 1977), and it is measured with a good signal-to-noise in our instrument. In A16, we describe the procedure of the gain calibration as built in the analysis pipeline. The output of this procedure is the “gain”  $G(\lambda)$  (Eq. C.2 in A16), or the conversion between the instrument-recorded values (ADU) and the physical surface temperature (K). In the left panel of Figure B3 we show the gain calculated as a function of frequency from Cassiopeia A measurements taken throughout the Science Verification period. We again see the characteristic standing-wave patterns similar to that seen in the beam size. The variation over this time period is roughly at the 10% level.

We can then continue to estimate the on-sky system temperature by dividing the baseline level of the data (the smooth background without astronomical sources and RFI) by  $G(\lambda)$ . With the Cassiopeia A measurements shown in the right panel of Figure B3, we derive the median system temperature as shown in Figure 6. As discussed in A16, the system temperature fluctuates at the few K level and mainly comes from the temperature fluctuation in the horn and other exposed, non-regulated components. These will be improved upon in the future.